BNL-203478-2018-JAAM

# Photoactivatable fluorescent probes reveal heterogeneous nanoparticle permeation through biological gels at multiple scales

B. S. Schuster, D. B. Allan

To be published in "JOURNAL OF CONTROLLED RELEASE"

August 2017

Photon Sciences

**Brookhaven National Laboratory**

**U.S. Department of Energy**

USDOE Office of Science (SC), Basic Energy Sciences (BES) (SC-22)

# DISCLAIMER

# Photoactivatable fluorescent probes reveal heterogeneous nanoparticle permeation through biological gels at multiple scales

Benjamin S. Schuster[a,b,1,2], Daniel B. Allan[c,d,1], Joshua C. Kays[a,b,1], Justin Hanes[a,b,e,*], Robert L. Leheny[c,**]

[a] Center for Nanomedicine, Johns Hopkins University School of Medicine, Baltimore, MD 21231, USA
[b] Department of Biomedical Engineering, Johns Hopkins University School of Medicine, Baltimore, MD 21205, USA
[c] Department of Physics & Astronomy, Johns Hopkins University, Baltimore, MD 21218, USA
[d] NSLS-II, Brookhaven National Laboratory, Upton, NY 11973, USA
[e] Department of Ophthalmology, Johns Hopkins University School of Medicine, Baltimore, MD 21231, USA

ARTICLE INFO

*Keywords:*
Photoactivation
Fibrin
Cystic fibrosis
Nanoparticle
Drug delivery
Particle tracking
FRAP
Fluorescence microscopy
Diffusion

ABSTRACT

Diffusion through biological gels is crucial for effective drug delivery using nanoparticles. Here, we demonstrate a new method to measure diffusivity over a large range of length scales – from tens of nanometers to tens of micrometers – using photoactivatable fluorescent nanoparticle probes. We have applied this method to investigate the length-scale dependent mobility of nanoparticles in fibrin gels and in sputum from patients with cystic fibrosis (CF). Nanoparticles composed of poly(lactic-*co*-glycolic acid), with polyethylene glycol coatings to resist bioadhesion, were internally labeled with caged rhodamine to make the particles photoactivatable. We activated particles within a region of sample using brief, targeted exposure to UV light, uncaging the rhodamine and causing the particles in that region to become fluorescent. We imaged the subsequent spatiotemporal evolution in fluorescence intensity and observed the collective particle diffusion over tens of minutes and tens of micrometers. We also performed complementary multiple particle tracking experiments on the same particles, extending significantly the range over which particle motion and its heterogeneity can be observed. In fibrin gels, both methods showed an immobile fraction of particles and a mobile fraction that diffused over all measured length scales. In the CF sputum, particle diffusion was spatially heterogeneous and locally anisotropic but nevertheless typically led to unbounded transport extending tens of micrometers within tens of minutes. These findings provide insight into the mesoscale architecture of these gels and its role in setting their permeability on physiologically relevant length scales, pointing toward strategies for improving nanoparticle drug delivery.

## 1. Introduction

Nanoparticles hold considerable potential as vehicles for controlled release and targeted delivery of drugs [1]. To achieve therapeutic efficacy, drug-loaded nanoparticles often must diffuse through biological barriers [2–9]. In some instances, the barrier is only a few micrometers thick, as in the case of tear film at the ocular surface [10,11]. In other instances, nanoparticles must penetrate tens of micrometers or more through viscoelastic biological gels or tissue [2,5,9,12]. Measurements of nanoparticle mobility in vitro at these physiologically relevant length scales are valuable for designing particles that exhibit favorable in vivo biodistribution [5–7]. Traditional techniques, such as diffusion chambers, are being replaced by fluorescence microscopy techniques that provide more accurate measurements without perturbing fluid balance or damaging delicate biological specimens, as reviewed elsewhere [3,13].

Here, we introduce a novel fluorescence microscopy strategy for measuring nanoparticle mobility in biological gels at multiple physiologically relevant length scales by employing biodegradable, adhesion-resistant nanoparticles containing a photoactivatable ("caged") fluorescent dye. This functionality enables the photoactivation of particles in a selected region of a sample and subsequent characterization of their

* Correspondence to: J. Hanes, Center for Nanomedicine, Wilmer Eye Institute, Johns Hopkins University School of Medicine, 400 N. Broadway, Robert H. and Clarice Smith Building, 6th Floor, Baltimore, MD 21231, USA.
** Correspondence to: R. L. Leheny, Department of Physics & Astronomy, Johns Hopkins University, 3400 N. Charles Street, Baltimore, MD 21218, USA.
*E-mail addresses:* hanes@jhmi.edu (J. Hanes), leheny@jhu.edu (R.L. Leheny).
[1] These authors contributed equally.
[2] Present address: Department of Bioengineering, University of Pennsylvania, Philadelphia, PA 19104, USA.

mobility as they spread over tens of micrometers. We call this technique PANDA, for photoactivatable nanoparticle diffusion assay. Extending this range, the motion of individual photoactivated particles can also be examined at high resolution – down to tens of nanometers – using multiple particle tracking (MPT). We have employed PANDA to provide new insight into nanoparticle permeation through biomedically important materials – including fibrin gels and cystic fibrosis (CF) patient sputum – whose adhesive components and mesh architecture pose barriers to drug delivery.

Our approach of using PANDA in conjunction with MPT has a number of advantages over existing fluorescence methods for measuring nanoparticle diffusivity. By itself, MPT is a powerful technique for analyzing many individual particle trajectories, and it has been adopted recently to measure nanomedicine transport in biological materials [14]. However, high-precision MPT requires microscope objectives with large numerical aperture and thus small depths of field [14]. Therefore, particles diffusing in three dimensions can typically be tracked for only several micrometers before diffusing out of focus [15,16]. In heterogeneous materials, diffusivities measured at small length scales might not agree with those measured at larger scales [17,18], and this difference can have important implications in assessing the efficacy of drug delivery strategies. The PANDA method permits direct observation of percolation through biological gels over longer length and time scales but sacrifices spatiotemporal and single-particle resolution. Hence, as we show, MPT and PANDA are complementary and together permit multiscale characterization of diffusion that provides insight into gel microstructure. PANDA also offers advantages over its inverse, fluorescence recovery after photobleaching (FRAP) [19–21], which has been used in drug delivery research for more than two decades [22,23], including for studying nanoparticle diffusion in biological gels [24–26]. Photoactivation generally provides better contrast and signal-to-noise ratio, with signal from the activated fluorophores appearing against a black background [27–29]. Photoactivation can require lower laser dosage than FRAP [27,29], especially in cases of fluorescent nanoparticles, which are often difficult to bleach. Finally, the ability to pattern photoactivated regions with a laser affords PANDA greater control and precision compared to directly microinjecting particles and observing their spread [12].

To date, fluorescence photoactivation has been employed primarily in cell biology [29–32], but one recent paper reported photoactivation experiments investigating molecular diffusion in cellulose-derived gels for microbicide delivery [18]. Our overarching goal here is to extend the application of fluorescence photoactivation and harness it for the study of nanoparticle diffusion through biological gels. One specific aim of this paper is to demonstrate that PANDA can quantify the fluorescent particles' spread over long distances and, importantly, that it is well-suited to observe spatial heterogeneities in diffusion. A second, critical aim of our work is to extend our knowledge of microscale diffusion from MPT measurements into the mesoscale.

As a proof of principle, Section 3.2 presents a comparison of MPT and PANDA measurements on particles diffusing in water. Section 3.3 then describes the application of the methods to fibrin, a protein gel whose microstructure and selective permeability are closely linked to its function, since fibrin forms the scaffolding of blood clots and plays a critical role in hemostasis [33,34]. In these measurements, both MPT and PANDA revealed mobile and immobile populations of particles in fibrin. Finally, in Section 3.4 we examine nanoparticle diffusion in sputum collected from CF patients [35,36]. Secretions coating the airway epithelium pose a major barrier to inhaled nanomedicine for lung diseases such as CF, but particles that can rapidly diffuse through this biological gel may avoid mucociliary clearance and achieve improved distribution, retention, and efficacy in the lungs [36–38]. The airway-surface liquid layer can range from a few micrometers to tens of micrometers thick, depending on location in the lungs and the disease state [39–41]. Employing PANDA, we characterized particle diffusivity in sputum over distances relevant to drug delivery in the lungs, and furthermore, revealed heterogeneities in particle mobility that might be missed with techniques surveying motion over only one length scale.

## 2. Materials and methods

### 2.1. Materials

Cholalic acid sodium salt (CHA) and NVOC$_2$-5-carboxy-Q-rhodamine-NHS ester (caged rhodamine-NHS ester) were purchased from Sigma-Aldrich (St. Louis, MO). Poly(lactide-*co*-glycolide(75:25)) amine endcap (PLGA-NH$_2$), $M_n$ 10–15 kDa was purchased from PolySciTech (West Lafayette, IN). Poly(lactide-*co*-glycolide(67:33))-polyethylene glycol diblock copolymer (PLGA-PEG; 45 kDa PLGA block and 5 kDa PEG block) was custom-synthesized by Jinan Daigang Biomaterial Co., Ltd. (Jinan, China). Human α-thrombin (activity 3059 NIH U/mg) and human fibrinogen (plasminogen depleted, activity 100%), both purified from human plasma, were purchased from Enzyme Research Laboratories (South Bend, IN; catalog numbers HT 1002a and FIB 1, respectively).

### 2.2. Nanoparticle formulation and characterization

#### 2.2.1. Labeling of PLGA with caged rhodamine

Caged rhodamine-NHS ester and PLGA-NH$_2$ were conjugated through formation of an amide bond. (Conjugating the dye to polymer in this way, rather than encapsulating the dye in the particles, reduces the likelihood of free dye being released.) Briefly, 90 mg of PLGA-NH$_2$ was added to 5 mg of caged rhodamine-NHS ester, leading to a slight molar excess of dye compared to PLGA, 1.23:1, and put under vacuum for 1 h. The mixture was then flushed with nitrogen gas, dissolved in 500 μL of anhydrous dichloromethane (DCM), and reacted for 12 h at room temperature under nitrogen gas. Additional DCM was added as needed to facilitate transfer into 10 mL of −20 °C diethyl ether to precipitate the product. The PLGA, now conjugated with the caged rhodamine, was washed twice in cold ether by centrifugation. Excess ether was decanted and the final product, the purified PLGA-caged rhodamine, was placed in a lyophilizer (FreeZone 4.5 Plus; Labconco) for 12 h. The dried product was stored at −20 °C in a shielded container to prevent exposure to incident UV light. It is important to note that the amide bond is formed between the amine end-cap of the PLGA and the succinimidyl (NHS) ester on the rhodamine; that is, the dye itself and not the ortho-nitroveratryloxycarbonyl (NVOC) cage is directly conjugated to PLGA. Thus, when the photolytic reaction occurs upon exposure to UV light, only the caging group is cleaved, and free dye is not released [30,42].

#### 2.2.2. PLGA-PEG particle formulation

Photoactivatable PLGA/PLGA-PEG nanoparticles were prepared using the emulsion solvent evaporation method [43]. Briefly, a 40 mg mixture (19:1 by mass) of PLGA45k-b-PEG5k and PLGA-caged rhodamine was dissolved in 400 μL of DCM, making a 100 mg/mL solution. This solution was injected into an ice-cooled vial containing 5 mL of 0.5% CHA aqueous solution, and sonicated at 30% amplitude for 2 min using a 130 W probe sonicator (Sonics & Materials, Newtown, CT) to form an oil-in-water emulsion of the organic phase (polymer and DCM) in the aqueous phase, stabilized by the CHA surfactant. The emulsion was immediately added to 35 mL of 0.5% CHA solution and stirred at 600 rpm for at least 3 h to allow for complete particle hardening. During particle formation, the hydrophilic PEG partitioned to the surface of the emulsion drop, while the relatively hydrophobic PLGA remained in the interior, resulting in particles with a dense PEG coating of approximately 20 PEG chains per 100 nm$^2$ [43,44]. The final particle suspension was filtered through a 5 μm and then 0.45 μm syringe filter, then the particles were collected and washed three times via centrifugation at 20,000 g for 25 min. The final suspension in DI water was stored at 4 °C. Particles were typically used within 5 days of synthesis,

though we found the diameter and ζ-potential of the nanoparticles to be stable for up to 2 weeks when stored at 4 °C.

#### 2.2.3. Particle characterization

The diameter and ζ-potential of the nanoparticles were determined by dynamic light scattering and laser Doppler electrophoresis, respectively, using a Zetasizer Nano ZS90 (Malvern Instruments, Southborough, MA). For these measurements, the particles were suspended in 10 mM NaCl at pH 7.4. Transmission electron microscopy (TEM) images of dried particles were taken on standard 400 mesh copper TEM grids (Ted Pella, Redding, CA) with a Hitachi H7600 electron microscope (Hitachi HTA, Clarksburg, MD).

### 2.3. Sample preparation

#### 2.3.1. Fibrin

Fibrin gel was made from defrosted aliquots of thrombin and fibrinogen, both purified from human plasma. Studies of fibrin are frequently performed in vitro with purified fibrinogen and thrombin [33,34,45], and such gels have similar structures and mechanical properties as blood clots [46], though blood clots retrieved from patients do show patient-to-patient variability [47]. The thrombin solution was first prepared by adding nanoparticles, at concentrations appropriate for MPT and PANDA, to 2.22 U/mL thrombin in PBS. Then, 20 μL of 40 mg/mL fibrinogen was pipetted into 180 μL of the thrombin solution, yielding a 4 mg/mL concentration of fibrinogen and 2 U/mL thrombin [34]. This concentration was chosen for its physiological relevance, as 4 mg/mL is the approximate concentration of fibrinogen in human plasma [45]. Upon adding fibrinogen to thrombin, the mixture was immediately vortexed at high speed for 2 s to homogenize the solution. Then, 30 μL of the solution was immediately pipetted into a 30 μL well on a glass slide and covered with a glass coverslip. The coverslip and chamber were sealed together externally with a cyanoacrylate glue, making sure the glue never contacted the sample inside. The slide was then incubated at 37 °C for 20 min to ensure gelation. In all cases, slides were wrapped in aluminum foil to prevent premature exposure to UV light. For particle tracking, the final particle concentration in the gels was ~0.0001% by mass, and for PANDA experiments, the final concentration was approximately 0.19% by mass. These same particle concentrations were also used for experiments in water and CF sputum.

#### 2.3.2. Cystic fibrosis sputum (CFS)

Expectorated sputum was collected from adult cystic fibrosis patients at the Johns Hopkins Cystic Fibrosis Center Adult Clinic, under informed consent and in accordance with Johns Hopkins Medicine Institutional Review Board-approved protocols. Half of the patients were male and half were female; their age was 34 ± 10 (mean ± SD). Sputum samples were stored at 4 °C until use and were typically analyzed the day after collection. CFS slides were prepared as previously described [36,37]: 30 μL aliquots of CFS were withdrawn using a Wiretrol (Drummond Scientific Company, Broomall, PA) and dispensed into 30 μL wells on glass slides. Then, 1 μL of nanoparticles suspended in water were added to the sputum aliquot and stirred thoroughly yet gently with a 10 μL plastic pipette tip to mix in the particles without disrupting the structure of the CF sputum. Uniform dispersion of the particles in the sputum was confirmed by the uniformity in fluorescence of the illuminated region upon activation. We note similar sample mixing and preparation techniques have been employed by other researchers studying nanoparticle transport in mucus [17,24]. Furthermore, previous studies from our group have confirmed that mucus samples subjected to these manipulations retain their expected bulk rheological properties and recapitulate ex vivo the in vivo barrier properties of mucus gels to nanoparticles [35,37,48,49]. After the particles were introduced into the sputum, the slide was sealed with a glass coverslip and then incubated at room temperature for 1–2 h to prevent advection during imaging.

### 2.4. Nanoparticle transport measurements

#### 2.4.1. Multiple particle tracking

Particle tracking in the water, fibrin, and CF sputum samples was performed at room temperature using an inverted widefield epifluorescence microscope (Axio Observer; Carl Zeiss, Thornwood, NY) with a 100×/1.46 NA oil-immersion objective. Movies were collected with 19-ms exposure at 20 fps for 500 frames using an EMCCD camera (Evolve 512; Photometrics, Tucson, AZ). Particle motion was analyzed using custom-written MATLAB particle-tracking software based on the algorithm of Crocker and Grier [14,50].

#### 2.4.2. PANDA experiments

Fluorescence perturbation experiments were performed on a Zeiss LSM510 laser scanning confocal microscope (Carl Zeiss, Thornwood, NY). A 20× (Plan Apochromat, 0.75 NA) objective was used for the water and fibrin experiments, while a 63× (Plan Apochromat, 1.4 NA, oil immersion) objective was used for the CF sputum experiments to image the spatial heterogeneity of sputum with high resolution. All images were 512 by 512 pixels. A typical measurement began with collection of five background images. Then, the caged rhodamine encapsulated in the particles within a selected region of the sample was activated ("uncaged") by 5–20 iterations of a 405-nm laser at 100% power (25 mW). The activated region was 40 by 512 pixels for the water and fibrin experiments, corresponding to 35 by 449 μm, and was 60 by 512 pixels for the CF sputum experiments, corresponding to 16.7 by 143 μm. The time-dependent distribution of the fluorescent particles after photoactivation was then imaged every 1.5 s using a 543-nm laser (1 W) at 10–30% power, which excited the activated rhodamine, paired with a 560–615 nm bandpass filter for detection of the emitted fluorescence.

## 3. Results and discussion

### 3.1. Characterization of photoactivatable nanoparticles and overview of photoactivatable nanoparticle diffusion assay (PANDA)

We synthesized nanoparticles from poly(lactic-*co*-glycolic acid) (PLGA) and polyethylene glycol (PEG), two polymers used in FDA-approved products [51]. PLGA, which is biodegradable and has tunable encapsulation and release properties, formed the particle core. PEG, a hydrophilic and uncharged polymer, formed a dense coat on the particle surface. The particles were 160 nm in diameter with PDI 0.09 as determined by dynamic light scattering, had a near-neutral surface charge (Table S1), and had a spherical morphology as seen by transmission electron microscopy (Fig. 1A). PEG coatings on nanoparticles greatly reduce their adhesion to biological materials, so that sufficiently small PEG-coated particles can penetrate porous gels and tissues, in contrast to uncoated polymeric particles that are often adhesively immobilized and larger particles that may be sterically immobilized [6,33,35,37,52,53]. As an illustration, Fig. S1 displays a comparison of the mobilities of nanoparticles of different sizes and surface coatings in CF sputum obtained with MPT.

To enable particle diffusion measurements, we conjugated photoactivatable ("caged") rhodamine [30] to PLGA incorporated into the particle core. The particles fluoresced only after irreversible uncaging of the rhodamine by a brief exposure to UV or violet light. Macroscopically, particle suspensions in water were milky white before activation (Fig. 1B, left), but turned pink upon exposure to UV light (Fig. 1B, right). Microscopically, we photoactivated particles in a defined region of a specimen and observed the diffusion of fluorescent particles from that region over tens of micrometers and tens of minutes, all using laser scanning confocal microscopy, as depicted schematically in Fig. 1C. In conjunction with these PANDA measurements, we also

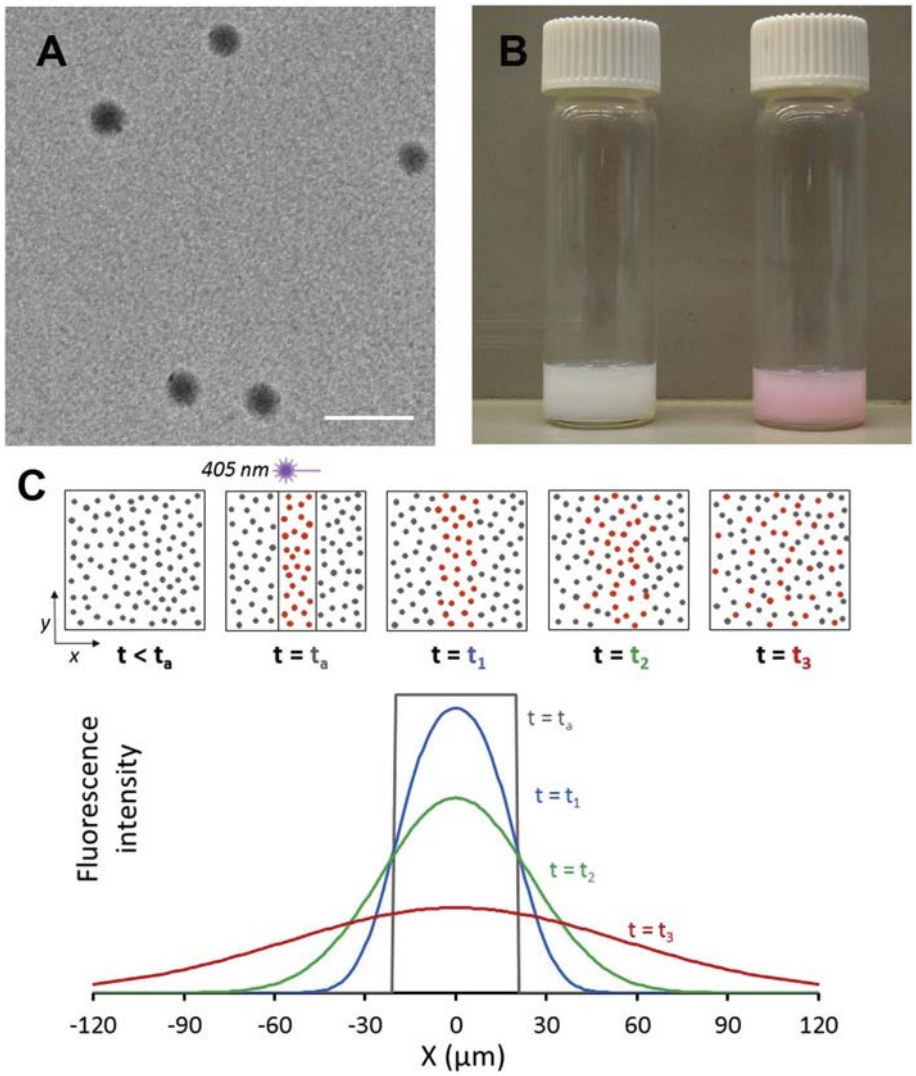


**Fig. 1.** Photoactivatable fluorescent nanoparticle probes. (A) Electron micrograph of photoactivatable PLGA-PEG nanoparticles after dehydration. Scale bar is 200 nm. Fully hydrated particles in buffer solution had a diameter of 160 nm, as measured by dynamic light scattering (Table S1). (B) Photograph of particle suspensions in water before (left vial) and after (right vial) UV light exposure, demonstrating activation of the caged rhodamine. (C) Schematic of a photoactivatable nanoparticle diffusion assay (PANDA) experiment, illustrating activation of fluorescence within a rectangular region by brief 405 nm laser irradiation and subsequent diffusion of activated particles from the region. Top row: Field of view before and after activation, showing particles diffusing over time. Bottom plot: Time-dependent fluorescence intensity along the *x*-direction.

tracked individual photoactivated particles at high spatial and temporal resolution by MPT.

### 3.2. Proof of concept

Both analytical [19,24,54,55] and numerical [56–58] methods have been used to analyze data from fluorescence perturbation experiments. Here, we employ a numerical approach to analyze the PANDA experiments, which offers two advantages: 1) It allows us to account for the measured initial activation profile, and 2) We obtain the mean squared displacement (MSD) from the PANDA data, which facilitates comparison with MPT data. As a proof of concept, we describe PANDA experiments to obtain the diffusivity $D$ of photoactivated nanoparticles in water from the evolution of the fluorescence intensity. Fig. 2A displays a set of images following photoactivation via 405 nm laser exposure to a 35-μm wide strip-shaped region of the sample, indicated by the red lines in the top image. From a series of such images, we obtain the fluorescence intensity $I(x, y, t)$, where $y$ is the direction parallel to the strip, $x$ is perpendicular to it, and $t$ is the time since photoactivation. For the particle concentrations in our experiments, $I(x, y, t)$ is linearly proportional to the concentration of activated particles $c(x, y, t)$ to good approximation.

To analyze $I(x, y, t)$ in water, we assume spatially homogeneous diffusion. (As discussed below, this assumption must be reconsidered for the biological gels.) Accordingly, we consider the average intensity profile $I(x,t) = \frac{1}{N}\sum I(x,y,t)$, where the sum is over the $N$ pixels along $y$ at fixed $x$. (In addition to diffusing in $x$, particles diffuse in $y$ and $z$. Our averaging is justified because diffusion in each direction is independent of the others. Diffusion in $z$ causes photoactivated particles to exit the focal volume in proportion to their concentration, which affects only the magnitude but not the shape of $I(x, y, t)$. Diffusion in $y$ causes the intensity near the edges at high and low $y$ to decrease over time. However, $I(x, y, t)$ as a function of $x$ at fixed $y$ and $t$ varies with $y$ only in magnitude and has a constant shape.) Fig. 2B shows $I(x, t)$ at the times following photoactivation corresponding to the images in Fig. 2A.

In a liquid like water, where particle mobility is dictated by the fluid's viscosity, the concentration evolves according to the diffusion equation (see ref. [59]). Thus, for any intensity distribution $I(x', t')$ at time $t'$, the distribution at some later time $t$ is

$$I(x,t) = \int_{-\infty}^{\infty} G(x - x'; t - t') I(x', t') dx' \tag{1}$$

where $G(x - x'; t - t')$ is the Gaussian,

$$G(x - x'; t - t') = \frac{1}{\sqrt{4\pi D(t - t')}} \exp\left[-\frac{(x - x')^2}{4D(t - t')}\right] \tag{2}$$

That is, the intensity profile at $t'$ can be mapped onto the profile at $t$ through convolution with a Gaussian of width $\sigma = \sqrt{2D(t - t')}$. Breakdown of this mapping would indicate non-diffusive motion, which is not expected in water but could occur in other materials.

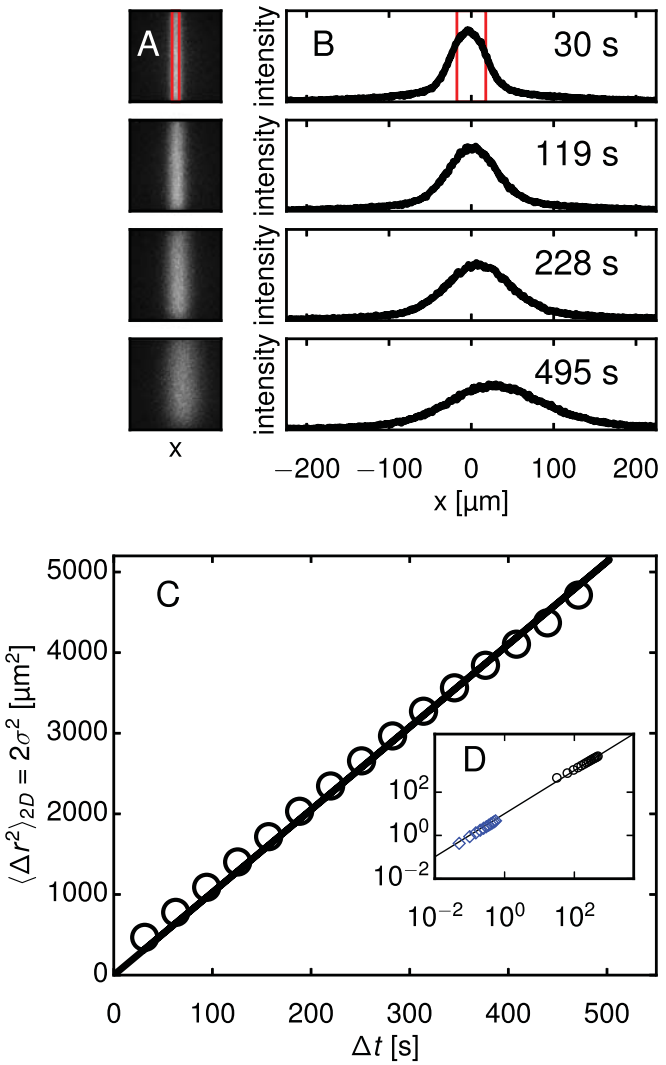


**Fig. 2.** Demonstration of technique: Diffusion of photoactivatable nanoparticles in water at multiple time and length scales. The PANDA technique permits measurements of diffusion over hundreds of seconds and tens of micrometers. (A) Fluorescence images of water containing nanoparticles are shown at four times following activation. The region outlined in red, which is 35 μm wide, was momentarily exposed to 405 nm laser light, making particles in that region fluorescent. Subsequent diffusion from the activation region was imaged using a 20× objective. (B) Intensity profiles are calculated by averaging the intensity of each column of the images. The intensity scale is the same in all plots. Convective drift is apparent, but the analysis is robust to this uniform motion. (C) Profiles at different times can be mapped onto each other through convolution with a Gaussian, as described in the text. The variance $\sigma^2(\Delta t)$ of the Gaussian that maps a given profile at any $t'$ onto the profile at $t = t' + \Delta t$ is related to the nanoparticles' diffusivity $D$ through $\sigma^2(\Delta t) = 2D\Delta t$. Since PANDA measures diffusion in one dimension and MPT measures diffusion in two dimensions, we multiply $\sigma^2$ by 2 to facilitate comparison between MPT and PANDA results. (D) Multiple particle tracking (MPT) of photoactivated particles permits measurements of diffusion at high spatiotemporal resolution over short time and length scales. For diffusive particles tracked in two dimensions, the mean squared displacement (MSD) is related to $D$ through $\langle \Delta r^2 \rangle = 4D\Delta t$. The ensemble-averaged MSD of the particle trajectories (blue diamonds) is shown along with the Gaussian variances from (C), plotted again as black circles. The diffusivity obtained from this PANDA experiment was $D = 2.56\ \mu m^2/s$, in good agreement with that obtained from MPT, $D = 2.31 \pm 0.08\ \mu m^2/s$, and from dynamic light scattering, $D = 2.64 \pm 0.10\ \mu m^2/s$. (For interpretation of the references to color in this figure legend, the reader is referred to the web version of this article.)

During a typical experiment, fluorescence images were collected for 10–30 min. The intensity profile was calculated for each image, and every profile was mapped onto each future profile through convolution with a Gaussian, as in Eq. (1). The width σ generating the most accurate mapping was determined using a nonlinear least-squares fit. Each mapping constituted a separate, though not strictly statistically independent, measurement of the MSD. Mappings corresponding to the same time interval $\Delta t = t - t'$ were averaged to produce $\sigma^2(\Delta t)$, shown in Fig. 2C, and $D$ was obtained through a linear regression to $\sigma^2(\Delta t)$. For the trial shown in Fig. 2, $D = 2.56\ \mu m^2/s$, which is representative of a set of 11 PANDA trials in water, for which $D = 2.68 \pm 0.34\ \mu m^2/s$ (mean ± standard deviation). Fig. 2D shows $\sigma^2(\Delta t)$ from PANDA along with the MSD $\langle \Delta r^2(\Delta t) \rangle$ from MPT, wherein we tracked > 1000 particles in water and obtained an ensemble-average $D = 2.31 \pm 0.08\ \mu m^2/s$, in agreement with the PANDA result and with the diffusivity measured by dynamic light scattering, $D = 2.64 \pm 0.10\ \mu m^2/s$. Two observations from these measurements confirm that dye did not leach from the particles during the photolytic reaction: First, there was no increase in background fluorescence after photoactivation, and second, $D$ agrees with the value expected based on the Stokes-Einstein relation for 160 nm particles in water. ($D$ would be orders of magnitude larger for free dye.) Fig. 2D also illustrates the range of the PANDA experiment, which is set primarily by the magnification employed during the fluorescence microscopy measurement. Tuning the magnification between 5× and 100×, we estimate the PANDA technique can characterize nanoparticle displacements from a maximum of approximately 1 mm down to a minimum on the order of 1 μm.

### 3.3. Fibrin

Fibrin forms the scaffolding of blood clots, so measuring the permeability of fibrin gels is important for understanding its role in wound healing and for designing effective thrombolytic agents for ischemic stroke and myocardial infarction. To this end, previous MPT studies [33,34] have characterized nanoparticle mobility in fibrin gels and have found that polymeric nanoparticles without PEG coatings become uniformly immobilized, whereas PEG-coated particles exhibit bimodal transport, with populations of mobile and immobile particles [33]. To gain a multiscale perspective on fibrin permeability, we have combined PANDA with MPT, asking specifically whether bimodal transport behavior of PEG-coated particles persists over longer, and more physiologically relevant, distances.

Indeed, in PANDA experiments on fibrin gels, we observed that some of the photoactivated nanoparticles could diffuse from the activation region, but others were immobile. This behavior is evident in Fig. 3A, which shows a series of images after photoactivation. The activation region remained bright and demarcated even at long times, indicating a population of localized nanoparticles, while some fluorescence intensity spread steadily outward. Fig. 3B, which depicts $I(x, t)$ corresponding to the images in Fig. 3A, reveals that the concentration profile approximates Gaussian tails outside the activation region but maintains a persistently large value within the region.

To distinguish these mobile and immobile populations in the analysis, we fit an intensity profile $I(x, t_f)$ at a late time $t_f$, to a Gaussian at values of $x$ outside the activation region and extrapolate through the region. The difference between the extrapolated profile and the measured intensities, which we interpret as due to the fluorescence from immobile particles, is assumed to be constant in time and is subtracted from $I(x, y, t)$ for all $t$. After identifying $I(x, y, t)$ of the mobile fraction in this way, we calculate $\sigma^2(\Delta t)$ of that fraction using the convolution method described above. The result is plotted in Fig. 3C alongside the MSDs of individual particles obtained from MPT. The MPT data indeed indicates two populations, split between mobile particles moving diffusively, $\langle \Delta r^2(\Delta t) \rangle \propto \Delta t$, and immobile particles, characterized by a finite asymptotic MSD, $\langle \Delta r^2(\Delta t \to \infty) \rangle = \langle \Delta r^2(\Delta t) \rangle_0$, that is near or below the tracking resolution limit. From MPT, we calculate $D = 1.70 \pm 0.12\ \mu m^2/s$ for the mobile fraction, which is compatible with $D = 2.45 \pm 0.20\ \mu m^2/s$ obtained for the mobile population in the PANDA experiments. This remarkably fast diffusion of the mobile particles in fibrin, with $D$ approximately 70–90% of that in water,

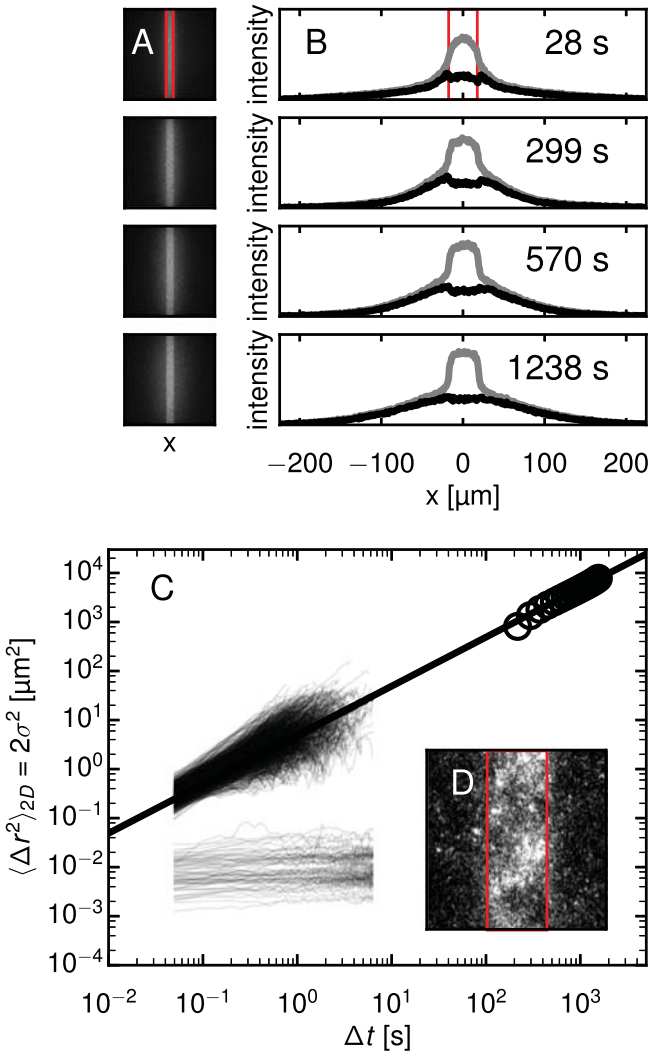


**Fig. 3.** PANDA and MPT show bimodal particle mobility in fibrin gels. (A) Images at four times from a PANDA experiment in fibrin using a 20× objective are shown. The activated region, outlined in red, is 35 μm wide. Approximately half the particles diffuse from the activated region while the rest remain localized, apparently confined in the gel. (B) The intensity profile due to the mobile population (black curve) at these time points is separated from the total intensity (gray curves) as described in the text. (C) The MSDs of 1149 individual particle trajectories from MPT are plotted along with $\sigma^2(\Delta t)$ of the mobile population from PANDA. The MSDs from MPT also fall into mobile and immobile populations. A best-fit line to the PANDA data, giving a diffusivity D = 2.45 ± 0.2 μm$^2$/s, passes through the mobile fraction of MSDs from MPT. (D) A view of an activated region of fibrin 1965 s after activation, imaged with a 40× objective, reveals a mottled pattern discussed in the text. Here, the width of the activation region, outlined in red, is 18 μm. (For interpretation of the references to color in this figure legend, the reader is referred to the web version of this article.)

agrees with the MPT results of Spero et al. on fibrin gels of similar composition [34]. As demonstrated above for water, MPT provides high-resolution trajectories of isolated particles over small distances, limited by the focal depth, whereas PANDA reveals transport of an ensemble of particles over longer distances at lower resolution. In conjunction, the two measurements span length scales ranging from tens of nanometers to tens of micrometers.

The bright fluorescence of the activated region persisted tens of minutes after photoactivation – even as the mobile particles diffused tens of micrometers from the region. The fluorescence intensity in the activation region appeared mottled at later times (> 1 min) following photoactivation, with brighter and darker domains of characteristic size of several micrometers, as illustrated in Fig. 3D. This spatial heterogeneity in the density of immobile particles provides evidence for the cause of their immobility in the fibrin. In particular, it indicates that the division of nanoparticles into mobile and immobile fractions does not result from variation among the particles in their tendency to adhere to the gel, since one would not expect the particles to be positioned during gel formation in such a correlated fashion based on their surface properties. Furthermore, recent studies have shown that PLGA-PEG nanoparticles synthesized by the same protocol as used here and containing a similar fraction of PEG are densely coated with PEG in a brush conformation and highly resistant to protein adhesion [44].

Instead, we infer that the heterogeneity in the density of immobile particles reflects mesoscale heterogeneity in the gel microstructure. Indeed, microscopy and light scattering studies on fibrin gels by Ferri and coworkers have shown micrometer-scale domains of higher fiber density interspersed with lower-density regions [60,61]. We conclude that the pore size of the high-concentration domains is smaller than the particles, such that the particles in these domains are trapped, whereas the particles in the lower-density domains of the gel diffuse freely. Significantly, the unbounded nature of this diffusion observed with PANDA indicates these domains form a percolating network accessible to the nanoparticles, a conclusion that could not be obtained from MPT or other more local probes. It is well established that fibrin gels have a bicontinuous structure that is central to their physiological role, with a network of fibers providing mechanical stiffness, and connected void spaces endowing the gels with permeability to proteins such as proteolytic enzymes for clot degradation [46,62]. Our results with PEG-coated nanoparticles in a model fibrin gel demonstrate that this permeability over large distances extends to nanoparticles. Our findings hence suggest that adhesion-resistant nanoparticles may be useful for uniform, sustained, local delivery of drugs, such as antimicrobial agents, to wounds [63].

### 3.4. *Cystic fibrosis sputum*

Particle-tracking studies have shown densely PEG-coated nanoparticles 200 nm in diameter and smaller can diffuse through cystic fibrosis sputum (CFS) over several micrometers [35,36]. (As shown in Fig. S1, uncoated particles of the same size are slowed by adhesion to CFS, and most particles 500 nm and larger are physically trapped.) In human lungs, the mucus barrier can range from several to tens of micrometers thick [40], so understanding whether therapeutic nanoparticles can traverse tens of micrometers to deliver their cargo to lung cells is important. Further, heterogeneity in nanoparticle mobility in CFS has been seen in MPT studies [36], and its impact on the long-distance transport relevant to drug delivery is unclear.

To address these issues, we conducted PANDA experiments on fresh sputum samples from four adult CF patients. On a basic level, we observed a significant fraction of nanoparticles diffusively traverse tens of micrometers in the samples from patients 1–3, while particle motion was highly localized in the sputum of patient 4 (Fig. S2). (Note, a higher magnification was employed in the PANDA measurements on CFS than in the water and fibrin experiments; the length scales probed were thus shorter but well suited to the distance of interest in CFS, which is a few tens of micrometers.) Many of the trials revealed mesoscale heterogeneity in the transport that breaks *y*-symmetry, wherein the spreading particles made greater progress in certain subregions and even showed pronounced anisotropy in their motion. Fig. 4 shows results from three PANDA trials, one from patient 1 and two from different locations in the sputum from patient 2, illustrating this behavior. Fig. 4A, C, and E show the final images of the three videos, 25 min after photoactivation. Fig. 4B, D, and F show contour plots illustrating the advancing front of fluorescent particles over time in those videos. The figures reveal spatial heterogeneity yet substantial regions of unbounded nanoparticle transport. They also illustrate the variation between patients and between locations within a single patient's sputum sample. As with the studies on fibrin, PANDA experiments hence reveal the underlying mesoscale heterogeneity of CFS and its role in setting permeability.

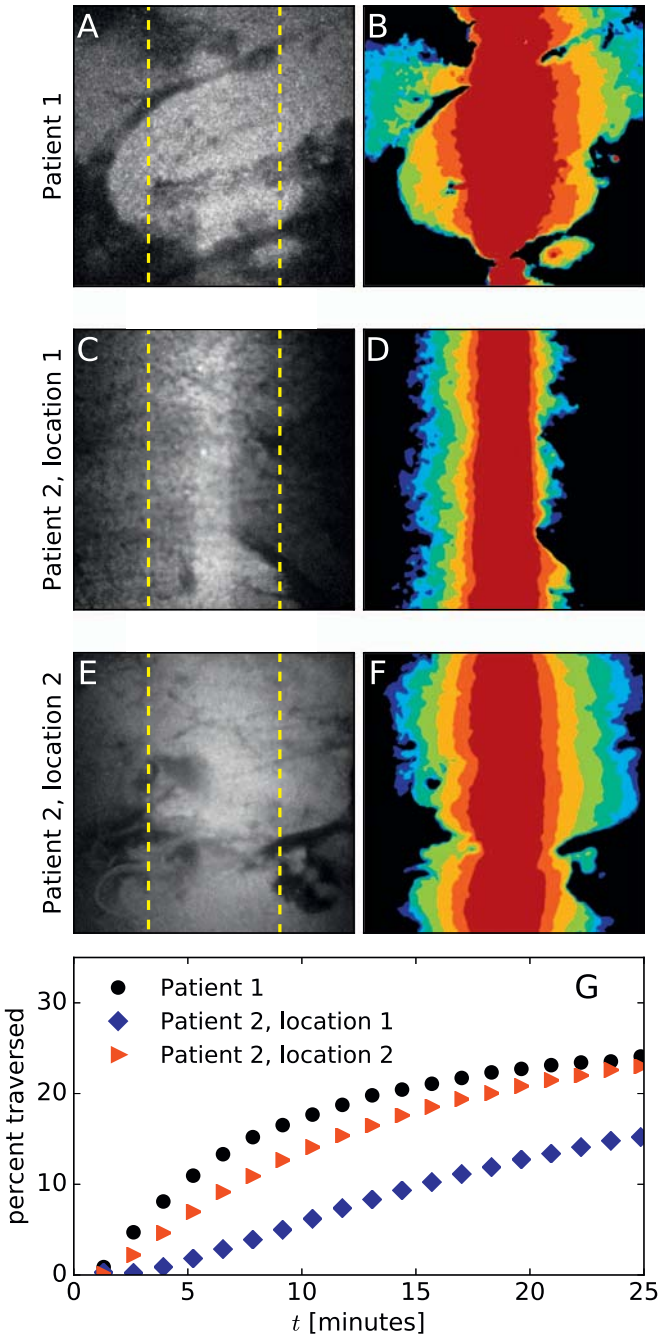


**Fig. 4.** Particle transport in cystic fibrosis sputum (CFS). Three representative PANDA experiments on sputum from CF patients, performed with a 63× objective, show nanoparticles diffusing tens of micrometers in tens of minutes. One video is from patient 1 and two videos are from patient 2, demonstrating heterogeneous behavior both between patients and within a single patient's sputum. (A, C, E) The final image from each video shows the fluorescence distribution approximately 25 min after photoactivation. Dashed yellow lines denote a distance of 25 μm from the activation region, which is 17 μm wide. (B, D, F) The spread of the particles is portrayed as a contour plot, with the colors from dark red to blue marking the advancing front of activated particles approximately 0.5, 2, 5, 10, 15, 20, and 25 min after photoactivation. To generate the contour plots, the images were smoothed using a Gaussian with σ = 3 pixels, and then thresholded using a threshold of 0.25 times the maximum pixel value. (G) The percentage of particles that have diffused at least 25 μm from the initial activation region – calculated as the percentage of total fluorescence intensity outside the dashed yellow lines in (A), (C), and (E) – is plotted as a function of time for each video. (For interpretation of the references to color in this figure legend, the reader is referred to the web version of this article.)

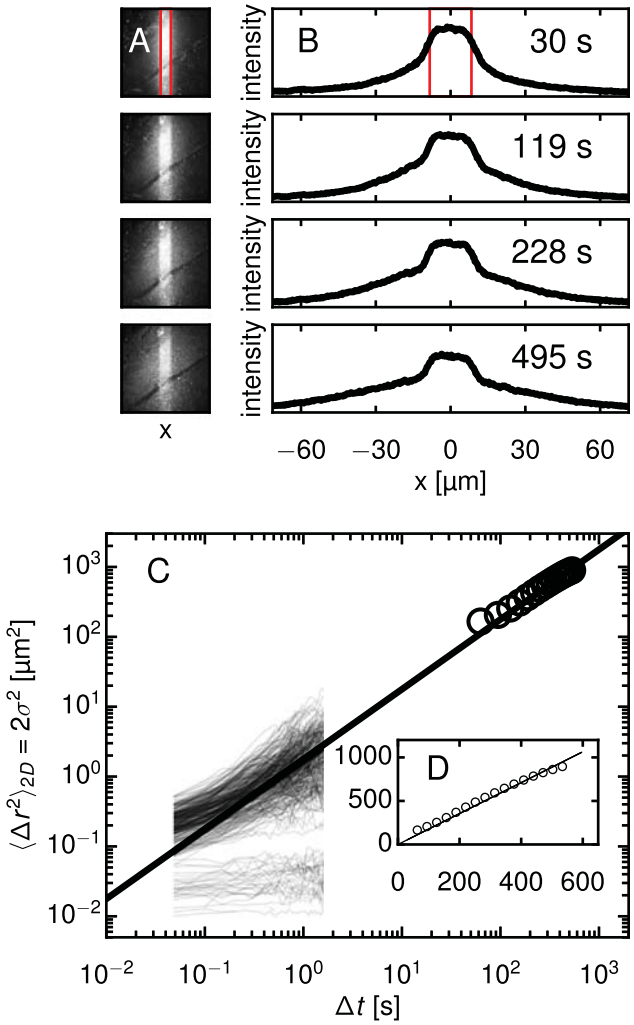


**Fig. 5.** PANDA and MPT diffusion measurements in CFS over multiple time and length scales relevant to drug delivery. (A) Four time points from a PANDA experiment in CFS, in which the evolution was sufficiently homogenous to permit analysis as in Fig. 2, are shown. The PANDA experiment was conducted using a 63× objective. The red lines denote the boundary of the activation region, which is 17 μm wide. (B) Profiles for the time points in (A) are calculated. The scale of the intensity is the same for all plots. (C) $\sigma^2(\Delta t)$ from PANDA is plotted along with MSDs of 273 individual particle trajectories from MPT in the same CFS sample. A best-fit line to the PANDA data, giving a diffusivity $D = 0.44 \pm 0.1\ \mu m^2/s$, passes through the mobile population of MSDs from MPT, whose ensemble-averaged diffusivity is $D = 0.49 \pm 0.18\ \mu m^2/s$. (D) A plot of the PANDA data and best-fit line on linear axes. (For interpretation of the references to color in this figure legend, the reader is referred to the web version of this article.)

To provide a practical metric for drug delivery, Fig. 4G displays the percentage of particles in the trials shown in Fig. 4A–F that traversed a distance ≥ 25 μm from the activation region as a function of time since activation. This metric reaches 15–25% by 25 min after photoactivation, demonstrating that PEG-coated nanoparticles can travel in CF sputum over physiological distances. Of course, the uneven permeability shown in Fig. 4A–F implies delivery will likely be uneven across regions of the lung. Further study is needed to determine whether smaller particles would exhibit more uniform penetration.

While the vast majority of PANDA trials on CFS showed dramatic heterogeneity as illustrated in Fig. 4, in a few trials the nanoparticle transport was sufficiently homogeneous to enable analysis like that performed on water. Fig. 5A shows a series of images, and Fig. 5B shows $I(x, t)$ at the same time points, from such a trial from patient 3. As with fibrin, a population of immobilized particles is apparent in Fig. 5. However, in contrast to the fibrin analysis, in this case the fraction of immobile particles is too small to subtract accurately. Therefore, we

apply the convolution method as for water to calculate $\sigma^2(\Delta t)$, which we find is approximately linear in time (Fig. 5D), a signature of diffusion. The resulting diffusion coefficient, $D = 0.44 \pm 0.1\ \mu m^2/s$, is about one-sixth that of the same particles in water. In comparison, the bulk viscosity of CF sputum at low shear rates is $> 10^4$ times that of water, implying the diffusive PLGA-PEG nanoparticles are small enough relative to the mucus mesh that they do not experience the bulk viscosity [35,64]. Fig. 5C plots $\sigma^2(\Delta t)$ from PANDA alongside the MSDs of individual particles from MPT, also from patient 3. The MPT data shows a broad distribution of MSDs, similar to that seen in previous MPT studies on CFS [35], that nonetheless is consistent with the best-fit line through the PANDA data. Excluding the localized particles whose MSDs reach a plateau, we find the remaining mobile particles have an ensemble-averaged $D = 0.49 \pm 0.18\ \mu m^2/s$, in good agreement with the PANDA result. Although this trial from patient 3 was unusual in the relatively homogeneous particle mobility it displayed, we believe this result for the particle diffusivity is indicative of the mobility in the other CFS trials. For instance, approximately 10% of particles in this trial traversed a distance $\geq 25\ \mu m$ from the activation region after 10 min, a result that is similar to those in the trials shown in Fig. 4G. (See Fig. S3.)

Overall, using PANDA, we have observed that our PEG-coated PLGA nanoparticles, with diameter $< 200$ nm, were typically capable of diffusing through distances of ten or more micrometers in CF sputum. While previous work with MPT has demonstrated particle mobility on shorter length scales [35,37,43,44], nanoparticle diffusion in human mucus over longer, physiologically important distances at rates needed for drug delivery was not previously observed. In particular, our conclusions contrast with those of Kirch et al. [17], who studied transport of PEG-coated nanoparticles in horse pulmonary mucus ex vivo by particle tracking and by observing permeation of magnetic particles through gel-filled capillaries in a magnetic field. They reported that a fraction of particles could penetrate the mucus over short distances probed by particle tracking; however, no particles penetrated the millimeter-scale distances of the capillary permeation technique. A future study that investigates this system using PANDA would help clarify the source of this discrepancy [65]. Likewise, our conclusions differ from those of Ernst et al., who recently argued that 200 nm diameter particles cannot passively diffuse through a mucus layer over physiological times and distances [66]. Ernst et al. arrived at their conclusion by developing a mathematical model and fitting it to MPT data, further highlighting the importance of actual measurements, such as using PANDA, that probe longer time and length scales. The results from our ex vivo experiments indicate PLGA-PEG particles are capable of overcoming the mucosal barrier in the human lung for improved retention, distribution, and ultimately efficacy.

## 4. Conclusion

We have demonstrated a novel microscopy method, based on photoactivatable fluorescent nanoparticles, for measuring nanoparticle diffusion in biological gels. By examining the fluorescence distribution after photoactivation, and by tracking individual particles, we have ascertained that PEG-coated particles with diameters $< 200$ nm are capable of permeating adhesive fibrin gels and cystic fibrosis patient sputum at multiple length scales relevant to drug delivery. In fibrin, we found that PLGA-PEG particle transport was bimodal, with populations of mobile and immobile particles at all scales. In CF sputum, we observed spatially heterogeneous particle diffusion that nevertheless typically led to unbounded transport exceeding 10 μm.

A main objective of this work has been to assess whether short-distance diffusion measurements from MPT agree with longer-distance diffusion measurements. This is a crucial question because complex fluids and gels can have distinct, non-uniform microscopic domains, so measurements at one length scale may not accurately predict behavior at other length scales [18]. Importantly, the PANDA technique has allowed us to conclude that, for both fibrin and CF sputum, the nanoparticle mobility behavior observed with MPT at the single micrometer length scale qualitatively agrees with transport behavior at the physiologically important length scales of tens of micrometers. This agreement is demonstrated by the fit lines running through the MPT and PANDA data in Figs. 3C and 5C. Our results thus show that – from the perspective of the 160 nm diameter PLGA-PEG particles used here – the porous microdomains of these gels are interconnected, allowing particles to percolate over long length scales. This finding is critical for workers in the field of nanomedicine who have designed mucosal drug delivery systems based on observations of rapid diffusion in MPT experiments.

However, we predict that in other scenarios, the results from MPT and PANDA will diverge, revealing length-scale-dependent mobility. A first test of this hypothesis would be to probe the same materials studied in this paper – or other physically or chemically crosslinked gels – with larger particles. Particles whose diameters are closer in size to the average mesh size of the fibrin or CFS gel network may diffuse locally, but ultimately be unable to percolate through the network [33]. MPT would show particle mobility over short distances, but PANDA would reveal that these larger particles are unable to traverse distances of tens of micrometers. A second system to test, with important implications for nanomedicine, would be solid tumors. Interstitial transport of nanoparticles in tumors is primarily determined by collagen content; tumors are highly heterogeneous, with some regions collagen-rich and others collagen-poor [2]. MPT may show rapid nanoparticle transport in the collagen-poor domains, while PANDA would elucidate whether those domains are sufficiently interconnected to allow longer length-scale permeability. We also anticipate that in some experimental systems, PANDA may reveal anomalous subdiffusion due to transient trapping, tortuosity, or weak binding of the nanoparticle to the medium [67]. For instance, anomalous subdiffusion of dextrans in the extracellular space of rodent brain slices has been recently reported [68]; it remains to be determined whether nanoparticles display similar behavior, which would have implications for drug delivery to the brain [6].

In conclusion, PANDA is a potentially powerful technique for nanomedicine research because it bridges the gap between MPT experiments and in vivo experiments. MPT experiments are straightforward, quantitative, and can often be conducted on specimens from human patients, but only provide data over short length scales. In vivo animal experiments are difficult and less quantitative but necessary for assessing biodistribution en route to clinical translation. The complementary information from PANDA and MPT will allow further refinement of nanoparticle formulations and characterization of their ability to overcome drug delivery barriers in vitro, prior to proceeding with in vivo experiments. In particular, as the results on fibrin gels and cystic fibrosis sputum described above illustrate, the spatial range and resolution of the PANDA technique are especially well matched for characterizing mesoscale heterogeneity in permeability, which is a key property of many biological gels, but is inaccessible to MPT alone.

## Conflict of interest

The mucus-penetrating particle technology described in this publication was developed at Johns Hopkins University and is licensed to Kala Pharmaceuticals. Justin Hanes is co-founder of Kala and currently serves as a consultant. He owns company stock, which is subject to certain restrictions under Johns Hopkins University policy. The terms of this arrangement are being managed by Johns Hopkins University in accordance with its conflict of interest policies.

## Acknowledgements

We thank S. Kuo for helpful discussions and M.E. Pease, R. Grebe, F. Yang, C. Schneider, A. Kim, J.S. Suk, and M. Kanzawa for assistance. We thank M. Boyle for collecting the sputum samples. This work was supported by the NIH (P01HL51811 and 2P30EY001765), the Cystic

Fibrosis Foundation (HANES07XX0), and the NSF (DMR-1610875).

## Appendix A. Supplementary data

Supplementary data to this article can be found online at http://dx.doi.org/10.1016/j.jconrel.2017.05.035.

## References


[1] O.C. Farokhzad, R. Langer, Impact of nanotechnology on drug delivery, ACS Nano 3 (2009) 16–20, http://dx.doi.org/10.1021/nn900002m.

[2] R.K. Jain, T. Stylianopoulos, Delivering nanomedicine to solid tumors, Nat. Rev. Clin. Oncol. 7 (2010) 653–664, http://dx.doi.org/10.1038/nrclinonc.2010.139.

[3] N.N. Sanders, S.C. De Smedt, J. Demeester, The physical properties of biogels and their permeability for macromolecular drugs and colloidal drug carriers, J. Pharm. Sci. 89 (2000) 835–849, http://dx.doi.org/10.1002/1520-6017(200007)89:7<835::AID-JPS1>3.0.CO;2-6.

[4] J.R. Weiser, W.M. Saltzman, Controlled release for local delivery of drugs: barriers and models, J. Control. Release 190 (2014) 664–673, http://dx.doi.org/10.1016/j.jconrel.2014.04.048.

[5] E. Nance, C. Zhang, T.-Y. Shih, Q. Xu, B.S. Schuster, J. Hanes, Brain-penetrating nanoparticles improve paclitaxel efficacy in malignant glioma following local administration, ACS Nano 8 (2014) 10655–10664, http://dx.doi.org/10.1021/nn504210g.

[6] E.A. Nance, G.F. Woodworth, K.A. Sailor, T.-Y. Shih, Q. Xu, G. Swaminathan, D. Xiang, C. Eberhart, J. Hanes, A dense poly(ethylene glycol) coating improves penetration of large polymeric nanoparticles within brain tissue, Sci. Transl. Med. 4 (2012) 149ra119 http://dx.doi.org/10.1126/scitranslmed.3003594.

[7] L.M. Ensign, B.C. Tang, Y.-Y. Wang, T.A. Tse, T. Hoen, R. Cone, J. Hanes, Mucus-penetrating nanoparticles for vaginal drug delivery protect against herpes simplex virus, Sci. Transl. Med. 4 (2012) 138ra79 http://dx.doi.org/10.1126/scitranslmed.3003453.

[8] O. Lieleg, I. Vladescu, K. Ribbeck, Characterization of particle translocation through mucin hydrogels, Biophys. J. 98 (2010) 1782–1789, http://dx.doi.org/10.1016/j.bpj.2010.01.012.

[9] L.M. Ensign, R. Cone, J. Hanes, Oral drug delivery with polymeric nanoparticles: the gastrointestinal mucus barriers, Adv. Drug Deliv. Rev. 64 (2012) 557–570, http://dx.doi.org/10.1016/j.addr.2011.12.009.

[10] K. Azartash, J. Kwan, J.R. Paugh, A.L. Nguyen, J.V. Jester, E. Gratton, Pre-corneal tear film thickness in humans measured with a novel technique, Mol. Vis. 17 (2011) 756–767.

[11] P.E. King-Smith, B.A. Fink, R.M. Hill, K.W. Koelling, J.M. Tiffany, The thickness of the tear film, Curr. Eye Res. 29 (2004) 357–368, http://dx.doi.org/10.1080/02713680490516099.

[12] R.G. Thorne, C. Nicholson, In vivo diffusion analysis with quantum dots and dextrans predicts the width of brain extracellular space, Proc. Natl. Acad. Sci. U. S. A. 103 (2006) 5567–5572, http://dx.doi.org/10.1073/pnas.0509425103.

[13] Y. Cu, W.M. Saltzman, Mathematical modeling of molecular diffusion through mucus, Adv. Drug Deliv. Rev. 61 (2009) 101–114, http://dx.doi.org/10.1016/j.addr.2008.09.006.

[14] B.S. Schuster, L.M. Ensign, D.B. Allan, J.S. Suk, J. Hanes, Particle tracking in drug and gene delivery research: state-of-the-art applications and methods, Adv. Drug Deliv. Rev. 91 (2015) 70–91, http://dx.doi.org/10.1016/j.addr.2015.03.017.

[15] I.Y. Wong, M.L. Gardel, D.R. Reichman, E.R. Weeks, M.T. Valentine, A.R. Bausch, D.A. Weitz, Anomalous diffusion probes microstructure dynamics of entangled F-actin networks, Phys. Rev. Lett. 92 (2004) 178101, http://dx.doi.org/10.1103/PhysRevLett.92.178101.

[16] D.B. Hill, P.A. Vasquez, J. Mellnik, S.A. McKinley, A. Vose, F. Mu, A.G. Henderson, S.H. Donaldson, N.E. Alexis, R.C. Boucher, M.G. Forest, A biophysical basis for mucus solids concentration as a candidate biomarker for airways disease, PLoS One 9 (2014) e87681, http://dx.doi.org/10.1371/journal.pone.0087681.

[17] J. Kirch, A. Schneider, B. Abou, A. Hopf, U.F. Schaefer, M. Schneider, C. Schall, C. Wagner, C.-M. Lehr, Optical tweezers reveal relationship between microstructure and nanoparticle penetration of pulmonary mucus, Proc. Natl. Acad. Sci. U. S. A. 109 (2012) 18355–18360, http://dx.doi.org/10.1073/pnas.1214066109.

[18] A.R. Geonnotti, M.J. Furlow, T. Wu, M.G. DeSoto, M.H. Henderson, P.F. Kiser, D.F. Katz, Measuring macrodiffusion coefficients in microbicide hydrogels via postphotoactivation scanning, Biomacromolecules 9 (2008) 748–751, http://dx.doi.org/10.1021/bm701018w.

[19] D. Axelrod, D.E. Koppel, J. Schlessinger, E. Elson, W.W. Webb, Mobility measurement by analysis of fluorescence photobleaching recovery kinetics, Biophys. J. 16 (1976) 1055–1069, http://dx.doi.org/10.1016/S0006-3495(76)85755-4.

[20] M. Edidin, Y. Zagyansky, T.J. Lardner, Measurement of membrane protein lateral diffusion in single cells, Science 191 (1976) 466–468.

[21] N. Lorén, J. Hagman, J.K. Jonasson, H. Deschout, D. Bernin, F. Cella-Zanacchi, A. Diaspro, J.G. McNally, M. Ameloot, N. Smisdom, M. Nydén, A.-M. Hermansson, M. Rudemo, K. Braeckmans, Fluorescence recovery after photobleaching in material and life sciences: putting theory into practice, Q. Rev. Biophys. 48 (2015) 323–387, http://dx.doi.org/10.1017/S0033583515000013.

[22] S.R. Chary, R.K. Jain, Direct measurement of interstitial convection and diffusion of albumin in normal and neoplastic tissues by fluorescence photobleaching, Proc. Natl. Acad. Sci. U. S. A. 86 (1989) 5385–5389.

[23] H. Deschout, K. Raemdonck, J. Demeester, S.C. De Smedt, K. Braeckmans, FRAP in pharmaceutical research: practical guidelines and applications in drug delivery, Pharm. Res. 31 (2014) 255–270, http://dx.doi.org/10.1007/s11095-013-1146-9.

[24] K. Braeckmans, L. Peeters, N.N. Sanders, S.C. De Smedt, J. Demeester, Three-dimensional fluorescence recovery after photobleaching with the confocal scanning laser microscope, Biophys. J. 85 (2003) 2240–2252, http://dx.doi.org/10.1016/S0006-3495(03)74649-9.

[25] S.S. Olmsted, J.L. Padgett, A.I. Yudin, K.J. Whaley, T.R. Moench, R.A. Cone, Diffusion of macromolecules and virus-like particles in human cervical mucus, Biophys. J. 81 (2001) 1930–1937, http://dx.doi.org/10.1016/S0006-3495(01)75844-4.

[26] L. Peeters, N.N. Sanders, K. Braeckmans, K. Boussery, J. Van de Voorde, S.C. De Smedt, J. Demeester, Vitreous: a barrier to nonviral ocular gene therapy, Invest. Ophthalmol. Vis. Sci. 46 (2005) 3553–3561, http://dx.doi.org/10.1167/iovs.05-0165.

[27] A. Bancaud, S. Huet, G. Rabut, J. Ellenberg, Fluorescence perturbation techniques to study mobility and molecular dynamics of proteins in live cells: FRAP, photoactivation, photoconversion, and FLIP, Cold Spring Harb. Protoc. 2010 (2010) (pdb.top90).

[28] P.D. Calvert, J.A. Peet, A. Bragin, W.E. Schiesser, E.N. Pugh, Fluorescence relaxation in 3D from diffraction-limited sources of PAGFP or sinks of EGFP created by multiphoton photoconversion, J. Microsc. 225 (2007) 49–71, http://dx.doi.org/10.1111/j.1365-2818.2007.01715.x.

[29] G.H. Patterson, J. Lippincott-Schwartz, A photoactivatable GFP for selective photolabeling of proteins and cells, Science 297 (2002) 1873–1877, http://dx.doi.org/10.1126/science.1074952.

[30] K.R. Gee, E.S. Weinberg, D.J. Kozlowski, Caged Q-rhodamine dextran: a new photoactivated fluorescent tracer, Bioorg. Med. Chem. Lett. 11 (2001) 2181–2183.

[31] S.S. Agasti, R.H. Kohler, M. Liong, V.M. Peterson, H. Lee, R. Weissleder, Dual imaging and photoactivated nanoprobe for controlled cell tracking, Small 9 (2013) 222–227, http://dx.doi.org/10.1002/smll.201201007.

[32] J.C. Politz, Use of caged fluorochromes to track macromolecular movement in living cells, Trends Cell Biol. 9 (1999) 284–287.

[33] M.T. Valentine, Z.E. Perlman, M.L. Gardel, J.H. Shin, P. Matsudaira, T.J. Mitchison, D.A. Weitz, Colloid surface chemistry critically affects multiple particle tracking measurements of biomaterials, Biophys. J. 86 (2004) 4004–4014, http://dx.doi.org/10.1529/biophysj.103.037812.

[34] R.C. Spero, R.K. Sircar, R. Schubert, R.M. Taylor, A.S. Wolberg, R. Superfine, Nanoparticle diffusion measures bulk clot permeability, Biophys. J. 101 (2011) 943–950, http://dx.doi.org/10.1016/j.bpj.2011.06.052.

[35] J.S. Suk, S.K. Lai, Y.-Y. Wang, L.M. Ensign, P.L. Zeitlin, M.P. Boyle, J. Hanes, The penetration of fresh undiluted sputum expectorated by cystic fibrosis patients by non-adhesive polymer nanoparticles, Biomaterials 30 (2009) 2591–2597, http://dx.doi.org/10.1016/j.biomaterials.2008.12.076.

[36] B.S. Schuster, A.J. Kim, J.C. Kays, M.M. Kanzawa, W.B. Guggino, M.P. Boyle, S.M. Rowe, N. Muzyczka, J.S. Suk, J. Hanes, Overcoming the cystic fibrosis sputum barrier to leading adeno-associated virus gene therapy vectors, Mol. Ther. 22 (2014) 1484–1493, http://dx.doi.org/10.1038/mt.2014.89.

[37] B.S. Schuster, J.S. Suk, G.F. Woodworth, J. Hanes, Nanoparticle diffusion in respiratory mucus from humans without lung disease, Biomaterials 34 (2013) 3439–3446, http://dx.doi.org/10.1016/j.biomaterials.2013.01.064.

[38] A.J. Kim, N.J. Boylan, J.S. Suk, M. Hwangbo, T. Yu, B.S. Schuster, L. Cebotaru, W.G. Lesniak, J.S. Oh, P. Adstamongkonkul, A.Y. Choi, R.M. Kannan, J. Hanes, Use of single-site-functionalized PEG dendrons to prepare gene vectors that penetrate human mucus barriers, Angew. Chem. Int. Ed. Eng. 52 (2013) 3985–3988, http://dx.doi.org/10.1002/anie.201208556.

[39] S.E. Birket, K.K. Chu, L. Liu, G.H. Houser, B.J. Diephuis, E.J. Wilsterman, G. Dierksen, M. Mazur, S. Shastry, Y. Li, J.D. Watson, A.T. Smith, B.S. Schuster, J. Hanes, W.E. Grizzle, E.J. Sorscher, G.J. Tearney, S.M. Rowe, A functional anatomic defect of the cystic fibrosis airway, Am. J. Respir. Crit. Care Med. 190 (2014) 421–432, http://dx.doi.org/10.1164/rccm.201404-0670OC.

[40] J.V. Fahy, B.F. Dickey, Airway mucus function and dysfunction, N. Engl. J. Med. 363 (2010) 2233–2247, http://dx.doi.org/10.1056/NEJMra0910061.

[41] Y. Song, W. Namkung, D.W. Nielson, J.-W. Lee, W.E. Finkbeiner, A.S. Verkman, Airway surface liquid depth measured in ex vivo fragments of pig and human trachea: dependence on $Na^+$ and $Cl^-$ channel function, Am. J. Phys. Lung Cell. Mol. Phys. 297 (2009) L1131–L1140, http://dx.doi.org/10.1152/ajplung.00085.2009.

[42] L.M. Wysocki, J.B. Grimm, A.N. Tkachuk, T.A. Brown, E. Betzig, L.D. Lavis, Facile and general synthesis of photoactivatable xanthene dyes, Angew. Chem. Int. Ed. Eng. 50 (2011) 11206–11209, http://dx.doi.org/10.1002/anie.201104571.

[43] Q. Xu, N.J. Boylan, S. Cai, B. Miao, H. Patel, J. Hanes, Scalable method to produce biodegradable nanoparticles that rapidly penetrate human mucus, J. Control. Release 170 (2013) 279–286, http://dx.doi.org/10.1016/j.jconrel.2013.05.035.

[44] Q. Xu, L.M. Ensign, N.J. Boylan, A. Schön, X. Gong, J.-C. Yang, N.W. Lamb, S. Cai, T. Yu, E. Freire, J. Hanes, Impact of surface polyethylene glycol (PEG) density on biodegradable nanoparticle transport in mucus ex vivo and distribution in vivo, ACS Nano 9 (2015) 9217–9227, http://dx.doi.org/10.1021/acsnano.5b03876.

[45] A.R. Wufsus, K. Rana, A. Brown, J.R. Dorgan, M.W. Liberatore, K.B. Neeves, Elastic behavior and platelet retraction in low- and high-density fibrin gels, Biophys. J. 108 (2015) 173–183, http://dx.doi.org/10.1016/j.bpj.2014.11.007.

[46] P.A. Janmey, J.P. Winer, J.W. Weisel, Fibrin gels and their clinical and bioengineering applications, J. R. Soc. Interface 6 (2009) 1–10, http://dx.doi.org/10.1098/rsif.2008.0327.

[47] V.J. Marder, D.J. Chute, S. Starkman, A.M. Abolian, C. Kidwell, D. Liebeskind, B. Ovbiagele, F. Vinuela, G. Duckwiler, R. Jahan, P.M. Vespa, S. Selco, V. Rajajee, D. Kim, N. Sanossian, J.L. Saver, Analysis of thrombi retrieved from cerebral arteries of patients with acute ischemic stroke, Stroke 37 (2006) 2086–2093, http://

dx.doi.org/10.1161/01.STR.0000230307.03438.94.
[48] G.A. Duncan, J. Jung, J. Hanes, J.S. Suk, The mucus barrier to inhaled gene therapy, Mol. Ther. 24 (2016) 2043–2053, http://dx.doi.org/10.1038/mt.2016.182.
[49] C.S. Schneider, Q. Xu, N.J. Boylan, J. Chisholm, B.C. Tang, B.S. Schuster, A. Henning, L.M. Ensign, E. Lee, P. Adstamongkonkul, B.W. Simons, S.-Y.S. Wang, X. Gong, T. Yu, M.P. Boyle, J.S. Suk, J. Hanes, Nanoparticles that do not adhere to mucus provide uniform and long-lasting drug delivery to airways following inhalation, Sci. Adv. 3 (2017) e1601556, http://dx.doi.org/10.1126/sciadv.1601556.
[50] J.C. Crocker, D.G. Grier, Methods of digital video microscopy for colloidal studies, J. Colloid Interface Sci. 179 (1996) 298–310, http://dx.doi.org/10.1006/jcis.1996.0217.
[51] S.P. Schwendeman, R.B. Shah, B.A. Bailey, A.S. Schwendeman, Injectable controlled release depots for large molecules, J. Control. Release 190 (2014) 240–253, http://dx.doi.org/10.1016/j.jconrel.2014.05.057.
[52] S.K. Lai, D.E. O'Hanlon, S. Harrold, S.T. Man, Y.-Y. Wang, R. Cone, J. Hanes, Rapid transport of large polymeric nanoparticles in fresh undiluted human mucus, Proc. Natl. Acad. Sci. U. S. A. 104 (2007) 1482–1487, http://dx.doi.org/10.1073/pnas.0608611104.
[53] B.C. Tang, M. Dawson, S.K. Lai, Y.-Y. Wang, J.S. Suk, M. Yang, P. Zeitlin, M.P. Boyle, J. Fu, J. Hanes, Biodegradable polymer nanoparticles that rapidly penetrate the human mucus barrier, Proc. Natl. Acad. Sci. U. S. A. 106 (2009) 19268–19273, http://dx.doi.org/10.1073/pnas.0905998106.
[54] H. Deschout, J. Hagman, S. Fransson, J. Jonasson, M. Rudemo, N. Lorén, K. Braeckmans, Straightforward FRAP for quantitative diffusion measurements with a laser scanning microscope, Opt. Express 18 (2010) 22886–22905.
[55] J.C.G. Blonk, A. Don, H. Van Aalst, J.J. Birmingham, Fluorescence photobleaching recovery in the confocal scanning light microscope, J. Microsc. 169 (1993) 363–374, http://dx.doi.org/10.1111/j.1365-2818.1993.tb03312.x.
[56] A. Tannert, S. Tannert, S. Burgold, M. Schaefer, Convolution-based one and two component FRAP analysis: theory and application, Eur. Biophys. J. 38 (2009) 649–661, http://dx.doi.org/10.1007/s00249-009-0422-4.
[57] T.T. Tsay, K.A. Jacobson, Spatial Fourier analysis of video photobleaching measurements. Principles and optimization, Biophys. J. 60 (1991) 360–368, http://dx.doi.org/10.1016/S0006-3495(91)82061-6.
[58] P. Wedekind, U. Kubitscheck, O. Heinrich, R. Peters, Line-scanning microphotolysis for diffraction-limited measurements of lateral diffusion, Biophys. J. 71 (1996) 1621–1632, http://dx.doi.org/10.1016/S0006-3495(96)79366-9.
[59] J. Crank, The Mathematics of Diffusion, 2nd ed., Clarendon Press, Oxford, 1975.
[60] F. Ferri, M. Greco, G. Arcòvito, M. De Spirito, M. Rocco, Structure of fibrin gels studied by elastic light scattering techniques: dependence of fractal dimension, gel crossover length, fiber diameter, and fiber density on monomer concentration, Phys. Rev. E Stat. Nonlinear Soft Matter Phys. 66 (2002) 11913, http://dx.doi.org/10.1103/PhysRevE.66.011913.
[61] D. Magatti, M. Molteni, B. Cardinali, M. Rocco, F. Ferri, Modeling of fibrin gels based on confocal microscopy and light-scattering data, Biophys. J. 104 (2013) 1151–1159, http://dx.doi.org/10.1016/j.bpj.2013.01.024.
[62] A.E.X. Brown, R.I. Litvinov, D.E. Discher, P.K. Purohit, J.W. Weisel, Multiscale mechanics of fibrin polymer: gel stretching with protein unfolding and loss of water, Science 325 (2009) 741–744, http://dx.doi.org/10.1126/science.1172484.
[63] K.K. Chereddy, C.-H. Her, M. Comune, C. Moia, A. Lopes, P.E. Porporato, J. Vanacker, M.C. Lam, L. Steinstraesser, P. Sonveaux, H. Zhu, L.S. Ferreira, G. Vandermeulen, V. Préat, PLGA nanoparticles loaded with host defense peptide LL37 promote wound healing, J. Control. Release 194 (2014) 138–147, http://dx.doi.org/10.1016/j.jconrel.2014.08.016.
[64] L.-H. Cai, S. Panyukov, M. Rubinstein, Mobility of nonsticky nanoparticles in polymer liquids, Macromolecules 44 (2011) 7853–7863, http://dx.doi.org/10.1021/ma201583q.
[65] X. Murgia, P. Pawelzyk, U.F. Schaefer, C. Wagner, N. Willenbacher, C.-M. Lehr, Size-limited penetration of nanoparticles into porcine respiratory mucus after aerosol deposition, Biomacromolecules 17 (2016) 1536–1542, http://dx.doi.org/10.1021/acs.biomac.6b00164.
[66] M. Ernst, T. John, M. Guenther, C. Wagner, U.F. Schaefer, C.-M. Lehr, A model for the transient subdiffusive behavior of particles in mucus, Biophys. J. 112 (2017) 172–179, http://dx.doi.org/10.1016/j.bpj.2016.11.900.
[67] I.M. Sokolov, Models of anomalous diffusion in crowded environments, Soft Matter 8 (2012) 9043, http://dx.doi.org/10.1039/c2sm25701g.
[68] F. Xiao, J. Hrabe, S. Hrabetova, Anomalous extracellular diffusion in rat cerebellum, Biophys. J. 108 (2015) 2384–2395, http://dx.doi.org/10.1016/j.bpj.2015.02.034.